Dynamics of spherical tokamak plasma on the internal reconnection event

Naoki Mizuguchi
The Graduate University for Advanced Studies, Toki, Gifu 509-5292, Japan

Takaya Hayashi and Tetsuya Sato
The Graduate University for Advanced Studies, and Theory and Computer Simulation Center,
National Institute for Fusion Science, Toki, Gifu 509-5292, Japan

Nonlinear magnetohydrodynamic (MHD) simulations are executed to investigate the dynamical behavior of the relaxation phenomenon observed in spherical tokamak (ST) plasma that is known as the Internal Reconnection Event (IRE). The simulation results successfully reproduce several key features of IRE, and the physical mechanisms are revealed. A sudden collapse of the pressure profile takes place as a result of a nonlinear time development of a pressure-driven instability. A magnetic reconnection induced between the internal and the external magnetic field is found to play a crucial role in determining the nature of the overall process, namely, the rapid expulsion of the plasma heat energy due to the pressure imbalance along the reconnected field lines, and the large distortion in the overall shape. The resultant deformations in overall shape of the plasma are in good agreement with the experimental observations. © *2000 American Institute of Physics.* [S1070-664X(00)02203-5]

I. INTRODUCTION

The spherical tokamak (ST) experiments have demonstrated their promising properties, such as excellent stability and confinement at high β.[1–5] The START (Small Tight Aspect Ratio Tokamak) device at Culham[6] has achieved the highest average β of 40% in 1998.[7] Experimentally, the ST plasma has revealed several unique features in its dynamical behavior. The Internal Reconnection Event (IRE) is the most noticeable relaxation phenomenon, which is characterized by a collapse and a subsequent resilience of the pressure profile, the appearance of a positive spike in the net toroidal plasma current trace, and a large elongating distortion in the overall shape of plasma. IRE has been clearly observed in a couple of devices.[2,6] It is differentiated from the major disruptions in conventional tokamaks in that the plasma current is not terminated by IRE, and from the sawtooth oscillations in that IREs are observed with an increase of plasma current, and in irregular intervals. It should be noted, however, it has been observed in more recent experiments in START that IRE can sometimes lead to occurrence of current-terminating disruptions, especially after the divertor coils were installed close to the core plasma.[8]

The occurrence of IRE needs to be carefully considered when we aim to realize a fusion reactor by using the ST concept, partly because each time IRE occurs about 30% of the stored heat energy is lost, and partly because it can sometimes lead to an occurrence of major disruptions. The physical mechanisms of IRE have not been clarified well enough yet. To know them is an important and an urgent research topic for exploring larger scale ST devices.[1,9–11]

The advanced diagnostics has provided many clues for understanding the mechanisms of IRE. Before describing the simulation results, we review the phenomenology of IRE. As is shown in Fig. 10 of Ref. 12, which is the temporal variation in electron temperature and density profiles through an IRE measured by Thomson scattering in START, the central values fall in a short time scale of around $100 \sim 150 \, \mu$sec, and the radial profiles are broadened to the edge during an IRE. The experimental observations for the temporal change in the net toroidal current and the soft x-ray signal are plotted in Fig. 1.[13] An IRE usually proceeds in three stages in START experiments, namely, thermal quench, current increase, and current quench stages, which are referred to as I, II, and III in Fig. 1(b), respectively. Furthermore, the thermal quench stage usually proceeds in two steps, which are indicated by IA and IB, respectively, where the signal falls more slowly in the first (IA) step than the other (IB).[13]

In the START experiment, the overall structure of the plasma is monitored by using a CCD (charge coupled device) camera. Much fruitful information about the large-scale nonlinear behavior of plasma can be derived from the images. Some of the snapshots taken during an IRE are shown in Fig. 2,[13] in which the brighter region corresponds to relatively cold plasma. Figure 2(a) is taken by a monochromatic CCD camera, which has a higher time-resolution of about 30 μsec, at a moment corresponding to an early stage of IRE. A bright helical structure is observed to extend in the periphery from the top down to the bottom of the torus. It is noted that the structure exists only in a narrow region and is localized in the toroidal direction. Similar localized structures are often observed during IREs.[13] Figures 2(b)–2(d) are taken by a color CCD camera which has relatively poor time-resolution of about 100 μsec, which is comparable to the time scale of the fall of the peak pressure. Although instantaneous structures may be smoothed out, characteristic conical structures, which consist of multiple layers, are clearly seen at the top and the bottom of the torus in Fig. 2(b) (denoted by A). A filamentation structure is observed as bright stripes in the middle of the image (denoted by B). An overall distortion is captured in Figs. 2(c) and 2(d), which appears in the slightly
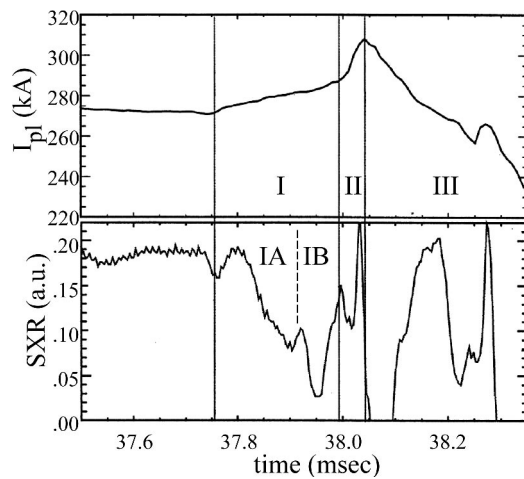
FIG. 1. Time development of the plasma current (top panel) and the soft x-ray signal which is measured at $R=34.6$ cm (bottom panel) for a typical IRE shot #36546 in the START experiment, by courtesy of Dr. M. Gryaznevich and Dr. A. Sykes. The different stages of an IRE are denoted by I (IA,IB), II, and III.

later stage of IRE. These two pictures were taken for different shots in the experiment, but are considered to capture the same phenomenon viewed from different angles perpendicular to each other. It can be seen in Fig. 2(c) that the shape of the poloidal cross section on both sides is largely tilted. In Fig. 2(d), the shape of the poloidal cross section is fat (horizontally elongated) in the right side of the image, and thin (vertically elongated) in the left. These axis-asymmetrical appearances imply the existence of an $m=2/n=1$ component, where m and n are the poloidal and the toroidal mode numbers, respectively.
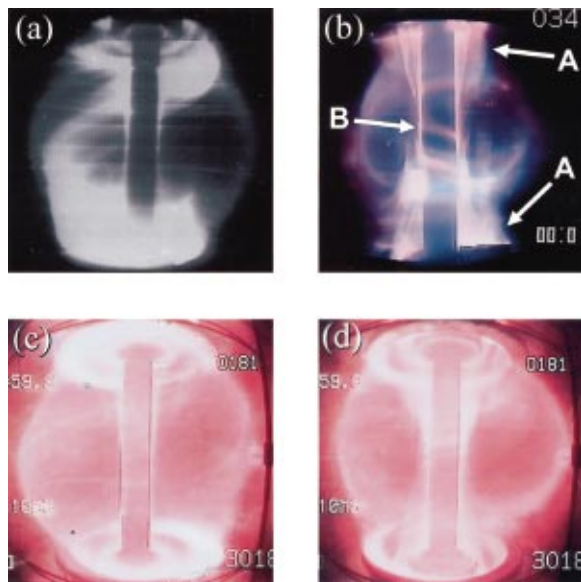

FIG. 2. (Color) CCD camera images of the START experiment when IRE is observed, by courtesy of Dr. M. Gryaznevich and Dr. A. Sykes. (a) Appearance of the localized deformation. (b) Appearance of the conical layers at the top and the bottom of the torus (denoted by A) and the filamentations (denoted by B). (c) Appearance of a tilted distortion. (d) Appearance of an axis-asymmetric distortion.

A model for describing IREs has been developed by Buttery *et al.* In Ref. 14, they reconstructed equilibrium using a free-boundary Grad-Shafranov code with the experimental data obtained in START. By comparing the pre- and the post-IRE states, they found out a conservation constraint in ''modified helicity.'' Scanning in various aspect ratios and falls in β_p using this constraint, they successfully explained the distinctive features of IRE such as disruption immunity at low aspect ratio.

Such is an outline of experimental observations and theoretical analyses of IREs. It can be summarized that an IRE is a relaxation phenomenon which accompanies a drastic change in overall shape in a short time scale, and is a highly nonlinear and fully three-dimensional phenomenon. It is necessary for understanding these complex features to make use of a nonlinear numerical simulation. In our previous simulation,[15] we have succeeded in reproducing several main features of an IRE such as a rapid fall in pressure and a large distortion in overall shape. In this paper, by advancing the analysis of the simulation result to a direct comparison with experimental results, the physical mechanisms of IRE are revealed.

There have been several nonlinear simulation works concerning disruption phenomena in a conventional tokamak. Kleva and Drake[16] studied the density limit disruption by using a fluid model including the edge radiation. They explained the pressure degradation by an injection of cold bubble as a result of nonlinear development of the $q=1$ kink mode, and succeeding relaxation between multiple $q=2$ modes. Park *et al.*[17] executed a nonlinear simulation to study high-β disruptions. They showed that toroidally localized high-n ballooning modes driven by a local pressure steepening due to evolution of low-n kink modes make a local pressure bulge and destroy the flux surfaces. In contrast, Kleva and Guzdar[18] claimed that a beta limit disruption can be driven by a dynamical process of high-n ballooning modes. IRE is different from these disruptions that occur in a conventional tokamak. The main difference is a large distortion in overall shape, and experimentally the property of the strong resiliency. In this paper, we investigate the nonlinear development of low-n modes in a simulation geometry in which the open external field is included to treat such a large deformation.

In Sec. II, the simulation model and the numerical method are introduced. The simulation results are presented in Sec. III. The comparisons between the simulations and the experiments, and some additional investigations, are discussed in Sec. IV. Finally, the results are summarized in the last section.

II. SIMULATION MODEL

The numerical simulations are executed in a three-dimensional full-toroidal geometry as shown in Fig. 3. The compressible nature in the governing equations is fully retained in the simulation model because of its importance in the nonlinear dynamics in this configuration. The governing
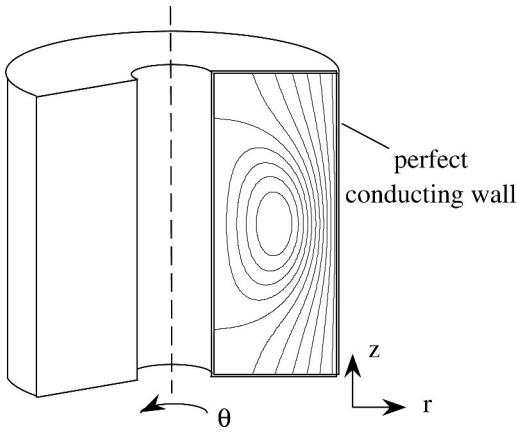
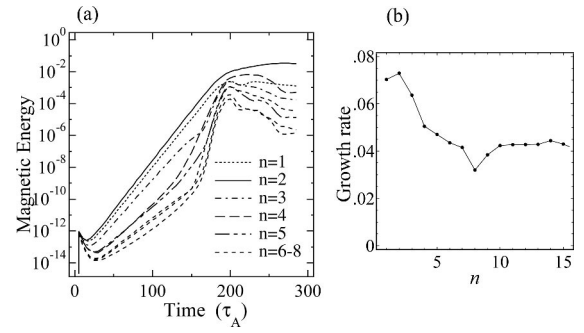FIG. 3. The schematic figure of the simulation system.

FIG. 4. (a) Time development of perturbation in the magnetic energy for each toroidal Fourier mode n in the simulation result. (b) Growth rate of the linear instability for each toroidal Fourier mode.

equations are the full set of normalized nonlinear resistive compressible magnetohydrodynamic (MHD) equations as follows:

$$\frac{\partial \rho}{\partial t} = -\nabla \cdot (\rho \mathbf{v}), \tag{2.1}$$

$$\frac{\partial}{\partial t}(\rho \mathbf{v}) = -\nabla \cdot (\rho \mathbf{v}\mathbf{v}) - \nabla p + \mathbf{j} \times \mathbf{B} \tag{2.2}$$

$$+ \mu \left(\nabla^2 \mathbf{v} + \frac{1}{3} \nabla(\nabla \cdot \mathbf{v}) \right), \tag{2.3}$$

$$\frac{\partial \mathbf{B}}{\partial t} = -\nabla \times \mathbf{E}, \tag{2.4}$$

$$\frac{\partial p}{\partial t} = -\nabla \cdot (p \mathbf{v}) - (\gamma - 1)(p \nabla \cdot \mathbf{v} + \eta \mathbf{j}^2 + \Phi), \tag{2.5}$$

$$\mathbf{j} = \nabla \times \mathbf{B}, \tag{2.6}$$

$$\mathbf{E} = -v \times \mathbf{B} + \eta \mathbf{j}, \tag{2.7}$$

$$\Phi = 2\mu \left(e_{ij} e_{ij} - \frac{1}{3}(\nabla \cdot \mathbf{v})^2 \right), \tag{2.8}$$

$$e_{ij} = \frac{1}{2} \left(\frac{\partial v_i}{\partial x_j} + \frac{\partial v_j}{\partial x_i} \right), \tag{2.9}$$

where ρ is the mass density, $\mathbf{v}$ is the velocity, $\mathbf{B}$ is the magnetic field, and p is the plasma pressure. The equations contain the resistivity η and the viscosity μ as uniform constants. The ratio of specific heats γ is 5/3.

The equations are solved in a cylindrical (r, θ, z) geometry with a rectangular poloidal cross section (see Fig. 3). The spatial derivatives of the equations are represented by the fourth-order finite differences and the time integration is calculated by the fourth-order Runge-Kutta method. The grid numbers are chosen to be $(N_r, N_\theta, N_z) = (128 \times 64 \times 128)$, which is large enough to treat the large-scale phenomena. The numerical soundness of the choice of the grid number and the time step has been confirmed by comparing results computed with coarser grid numbers or different time step. The initial condition is given by solving the Grad-Shafranov equation numerically under an assumption of polynomial

pressure and current profiles. It should be noted that the computation region includes both inside and outside the separatrix. An open magnetic field extends in the external region (see Fig. 3). The plasma pressure gradient exists only inside the separatrix in the initial condition. The external region is initially filled with a low temperature plasma, which equals 10% of that at the magnetic axis. The initial mass density is assumed to be uniform. The boundary condition is put as a perfect-conducting and no-slip wall at all boundaries of the computation region.

The variables are treated as a normalized form. Length, magnetic field, and mass density are normalized to the major radius of the geometrical center of the computation region, the toroidal field at the magnetic axis, and the initial mass density, respectively. Therefore, the unit of time equals the Alfvén transit time (τ_A) encircling the magnetic axis divided by 2π.

III. SIMULATION RESULTS

The simulation starts from a linearly unstable configuration which causes initial tiny perturbations to grow spontaneously. The perturbation is introduced on the plasma velocity field at $t=0$ as a random white noise. We have tried to execute the simulations under several conditions. A typical case, which well reproduces the properties of IRE, is presented in this section. The parameters used in the calculations are the aspect ratio $A=1.5$, the elongation $\kappa=1.9$, the central beta $\beta_0 = 44\%$, the full volume averaged beta $\langle \beta \rangle (\equiv \langle p \rangle / \langle B^2/2 \rangle) = 8.1\%$, the volume averaged beta with a commonly used definition $\beta_T (\equiv \langle p \rangle / B_0^2/2) = 12\%$, where B_0 is the vacuum field at the magnetic axis, and the central safety factor $q_0 = 0.91$. μ and η are assumed to be uniform values of 4×10^{-4} and 1×10^{-5}, respectively.

Shown in Fig. 4(a) is the time development of the perturbation in magnetic energy for each toroidal Fourier component. In the early stage of the growth (until $t=170\tau_A$), each of the components grows exponentially with its linear growth rate and phase independent of other components. Hereafter, we call it the ''linear stage.'' The subsequent time development may be called the ''nonlinear stage.''

Phys. Plasmas, Vol. 7, No. 3, March 2000

Dynamics of spherical tokamak plasma on the internal . . .   943
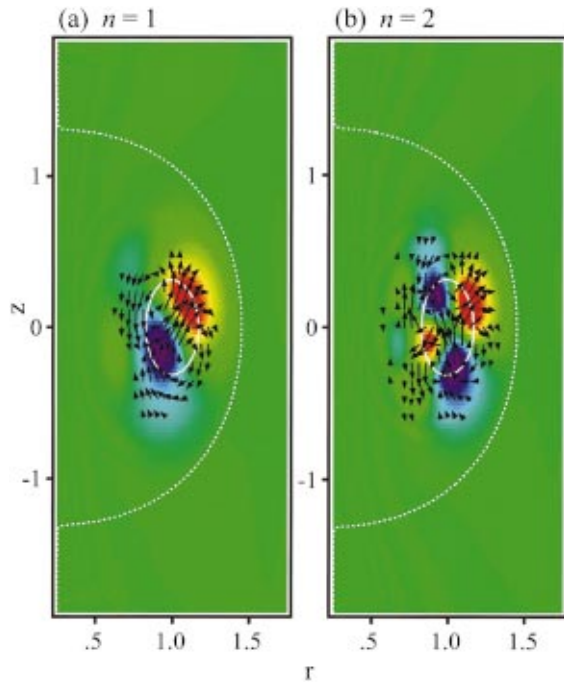

FIG. 5. (Color) Eigenfunction of the linear instability for (a) $n=1$ and (b) $n=2$ mode in the simulation result. The color shades represent the amplitude of the fluctuation in pressure. The arrows indicate the plasma flow. The location of the separatrix and the $q=1$ rational surface are denoted by dotted and solid curves, respectively.

TABLE I. Estimation of the driving source of the linear instability by the energy principle. All the values are normalized by the absolute value of the kink term for each mode. The negative value means destabilizing contribution, and the positive means stabilizing one. The expression for the lower three terms are referred to Ref. 19.

Term	$n=1$	$n=2$
Kink	−1	−1
Interchange	−6.6	−15.3
Alfvén	5.0	11.3
Fast magneto acoustic	0.7	0.8
Acoustic	0.4	1.2
Total	−1.4	−3.0

turbation of the magnetic field, respectively. All the equilibrium quantities are denoted by suffix 0. Substituting the eigenfunction obtained by the simulation for $\boldsymbol{\xi}$, we can estimate each term as listed in Table I with other stabilizing terms. Both of the kink and interchange terms are negative for both $n=1$ and $n=2$ modes, hence, they are driven by the combination of the current and the pressure gradient. However, the interchange term is much larger than the kink one in absolute value for each mode. Therefore, these modes are identified as pressure-driven modes. In addition, judging from the poloidal mode patterns shown in Fig. 5, which are not localized in the poloidal direction, it is concluded that these modes are not categorized into the ballooning mode but into the interchange mode.

A. Linear stage

The growth rate for each toroidal mode number (n) in the linear stage is plotted in Fig. 4(b). It can be seen that multiple numbers of eigenmodes are excited simultaneously and the growth rates come out to be larger for lower n modes. Particularly, the $n=1$ and $n=2$ modes have almost the same large growth rate. Since the initial perturbations include every mode with the same amplitude (white noise), the two modes dominate the growth with similar amplitude.

Figure 5 shows the poloidal mode structure for the $n=1$ and the $n=2$ modes. The variation of the color indicates the amplitude of the fluctuations in the plasma pressure. It can be clearly seen that the dominant poloidal components are $m=1$ for the $n=1$ mode and $m=2$ for the $n=2$ mode. The position of the $q=1$ rational surface drawn together in Fig. 5 suggests that these modes are resonant with it. The flow patterns are also drawn in Fig. 5. It can be seen that m pairs of vortices are formed on the poloidal cross section.

It is possible to identify the driving sources of these eigenmodes by estimating the kink and the interchange terms of the potential energy integral (δW) appearing in the energy principle.[19] These terms are expressed as

$$\delta W_{\text{kink}} = \frac{1}{2} \int d^3x \left\{ \frac{\mathbf{j}_0 \cdot \mathbf{B}_0}{|B_0^2|} \mathbf{B}_0 \times \boldsymbol{\xi} \cdot \widetilde{\mathbf{B}} \right\}, \tag{3.1}$$

$$\delta W_{\text{interchange}} = - \int d^3x \{ (\boldsymbol{\xi} \cdot \nabla p_0)(\boldsymbol{\xi} \cdot \boldsymbol{\kappa}) \}, \tag{3.2}$$

where $\boldsymbol{\xi}$, $\boldsymbol{\kappa}$, and $\widetilde{\mathbf{B}}$ denote the displacement vector, the normal curvature of the equilibrium magnetic field, and the per-

B. Nonlinear stage

Until the amplitude for each mode reaches a certain level (around 1×10^{-6} for the magnetic energy), the instabilities keep growing linearly with the growth rates and the mode structures fixed, as described in the previous subsection. The first sign of the nonlinearity appears as an abrupt change in the growth rate for the higher n modes. As seen in Fig. 4(a), the growth rate of the $n=4$ mode suddenly increases at $t=130\tau_A$. It is caused by the development of the higher harmonics for the $n=2$ mode and by the nonlinear couplings between the $n=1$ and the $n=3$ modes. In the early nonlinear stage, other higher n modes are also excited in the similar way. The growth of these nonlinear modes is so rapid that the fluctuation levels soon become significant enough to affect the global configuration. On the other hand, the growth rate of the $n=1$ and $n=2$ modes is saturated at around $t=190\tau_A$ as seen in Fig. 4(a).

The time evolution of the pressure profile in the early nonlinear stage is indicated in Fig. 6. The displacement becomes a visible scale at $t=165\tau_A$ [Fig. 6(b)]. The pressure profile is elliptically elongated in the poloidal cross section, reflecting the convection motion of the $m=2/n=2$ mode. At around $t=190\tau_A$ [Figs. 6(c)–6(d)], the deformation develops into a large bulge. The plasma pressure at the core region is transported from the core to the edge by such convection motions in a short time scale. The rapid fall of the central pressure observed in the experiments is explained by this mechanism. It is worthy of notice that although in the linear stage the instabilities have the nature of the internal modes, in the nonlinear stage they grow so much that even the out-
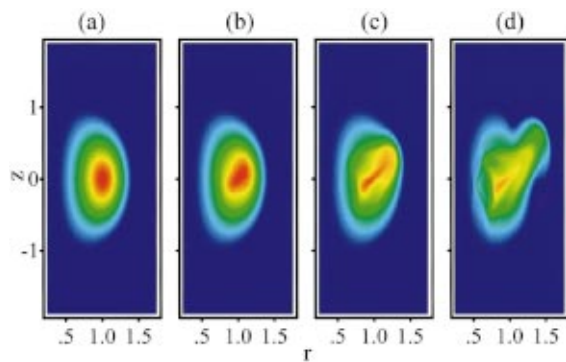
FIG. 6. (Color) Time development of pressure profile on a poloidal cross section in the simulation result for times equal to (a) 0, (b) 165, (c) 185, and (d) 200 τ_A.

FIG. 8. (Color) Magnetic reconnection between the internal and the external field. An identical magnetic field line and an iso-pressure surface near the separatrix are drawn for (a) $t=0$ and (b) $t=195\tau_A$. The magnetic field line is traced from a fixed point on the top boundary, and connects directly into the torus at $t=195\tau_A$.

ermost surface of the torus is deformed like an external mode. The three-dimensional view of the deformation of the torus at $t=195\tau_A$ is shown in Fig. 7 by a plot of an iso-surface of the pressure near the periphery of the torus. The structure of the surrounding magnetic field is also plotted in the figure by picking up typical external field lines. It can be clearly seen that toroidally localized deformation is formed as it pushes aside the neighboring magnetic field lines.

Due to the deformation of the surface, a large topological change in the configuration, namely, the magnetic reconnection, is induced on the surface of the torus. Shown in Fig. 8 is a magnetic field line at a different time traced from a fixed point on the top conducting wall boundary. A field line outside the separatrix never passes through the separatrix at $t=0$ [see Fig. 8(a)] because the initial equilibrium assumes the nested surfaces inside the torus. On the other hand, the field line traced at $t=200\tau_A$ [see Fig. 8(b)] penetrates into the inner region of the torus passing through around the localized deformation. It proves that a magnetic reconnection actually occurs between the internal and the external magnetic field. This reconnection process is schematically drawn in Fig. 9. A pair of field lines relevant to the magnetic reconnection (shown in red and blue lines) is almost parallel but not perfectly to each other, and lies on the opposite sides of the outermost surface [Fig. 9(a)]. One is the line inside the torus (red line) and the other is the open field line in the external region (blue line). The internal field lines are moved by the convective flow and pushed against the external field

just outside the bulge. The antiparallel fractions of the magnetic fields are driven to be reconnected [Fig. 9(b)] by enhancing a local current sheet.[20] Once the reconnection occurs, a part of the field lines in the torus is directly connected with the external field lines so that a strong plasma flow [as indicated with fat arrows in Fig. 9(c)] is generated by a large pressure imbalance along the reconnected field lines. The plasma outward flow is to be formed in pairs, for which the toroidal direction of the flow is opposite to each other. The plasma pressure is rapidly expelled out of the torus by those outward flows. This process is to be likened to putting a hole on the surface of a rubber ball which contains air with high pressure. The reconnected field lines, on the other hand, are somewhat bent just after the reconnection occurs, and are to be stretched by releasing the magnetic tension. It enhances the relevant field lines' distance from each other.

Along this schematic picture, we investigate the flow and the magnetic field structure in detail from the simulation result. Figure 10 shows the three-dimensional structures of the vector field of the plasma flow and the magnetic field lines. The magnetic field lines are colored depending on the local value of the plasma pressure. The field lines passing the localized deformation are emerging from the internal region and are connected to the external region. The pressure on them is definitely higher than that on other field lines which exist entirely on the external region. It implies that the plasma pressure actually flows out of the torus along the reconnected field lines. The flow field is colored in red and blue depending on the sign of the toroidal component of the velocity. It is clearly seen that two bunches of the flow are formed toward the top and the bottom of the torus originat-
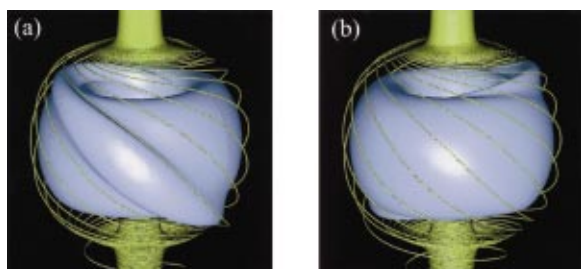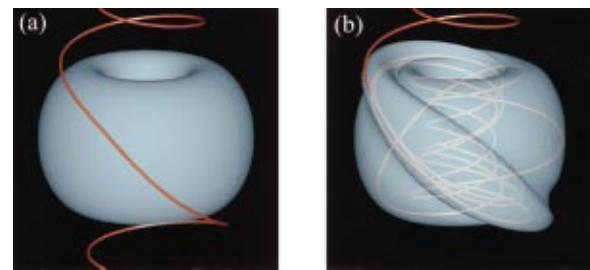

FIG. 7. (Color) Appearance of a localized deformation at $t=195\tau_A$ in the simulation result. (a) and (b) are viewed from the different angles of 180 deg apart from each other in the toroidal direction. The iso-pressure surface and the surrounding magnetic field lines are drawn.
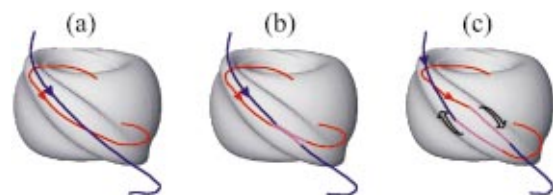

FIG. 9. (Color) Schematic figure for the dynamics of the magnetic reconnection between the external and the internal field. The external (blue) and the internal (red) field lines reconnect each other in the localized deformation. A pair of strong plasma flows passing each other in the localized deformation is formed along the large pressure gradient [seen in (c)].
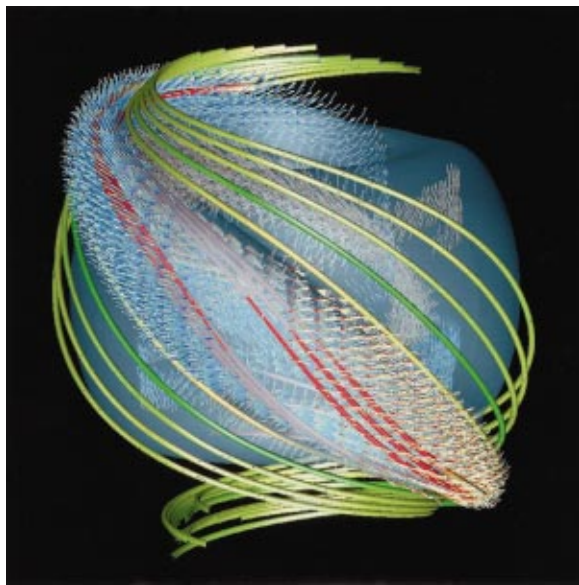
FIG. 10. (Color) Three-dimensional structure of plasma pressure, flow, and the magnetic field at $t=195\tau_A$ in the simulation result. The semitransparent surface indicates the iso-contour of plasma pressure, the fat curves are the arbitrary traces of magnetic field lines, and the thin lines represent the plasma flows. The direction of the flow is represented by the variation of the color on the lines [from the blue (red) to the white]. The difference between the blue and the red is the sign of toroidal velocity. The magnetic lines are colored in green to red as the local pressure increases.

ing from the inside of the torus. Interestingly, it is possible to go against the flows up to deep inside the torus. They cross each other at the localized deformation. These structures agree with the schematic picture shown in Fig. 9(c). The heat energy stored inside of the torus is ejected in this mechanism.

With this model, the expelled pressure is to expand quickly in a thin layer along the reconnected field lines. As is shown in Fig. 11, the pressure profile is changed into a thin conical structure at the top and the bottom of the torus. The global shape of the expelled plasma is deformed into a helically twisted structure along the external fields just outside the torus [Fig. 11(c)]. After $t=210\tau_A$, it becomes difficult to continue the computation, because the excited strong plasma flow makes highly irregular fine structures. However, the large-scale structure, which determines the subsequent time development, still remains. Here, we continue the simulation by removing the insignificant highly irregular fine structures, and aim to derive the large-scale behavior. A low-pass filtering technique based on a compensated binomial filter[21] is
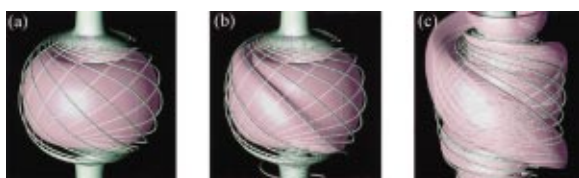

FIG. 11. (Color) Nonlinear time development of the three-dimensional structures of the plasma pressure represented by iso-pressure surfaces and the surrounding magnetic field lines. The time equals (a) 0, (b) 195, and (c) 250 τ_A.
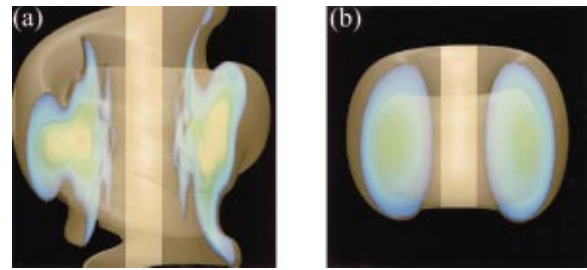

FIG. 12. (Color) Time development of the pressure profile in the latter stage of the simulation result at (a) $t=250$ and (b) $340\tau_A$.

applied at $t=200-345\tau_A$, to avoid the appearance of such irregular fine structures, which is assumed to correspond to enhancement of the anomalous dissipation mechanism. The subsequent time development is described below.

It should be pointed out that the basic structure of the torus is not disrupted even at this highly deformed stage. The outflow of pressure ceases when about 40% of the heat energy is lost. The modes which were unstable at the initial condition are stabilized at this stage, partly because of the change in the profile of the torus, especially the change in the safety factor profile, as is stated below, and partly because of the decrease in the β value due to the expulsion of the heat energy. After disappearance of the highly irregular structures, a torus-shaped structure appears again as shown in Fig. 12. The total kinetic energy falls to several percent compared to that of the most active stage at around $t=200\tau_A$. The pressure, current, and the safety factor profiles on the midplane at $t=345\tau_A$ are shown in Fig. 13. It can be seen that both the pressure and the current profiles become broader, and the maximum pressure decreases by about 50% compared to the initial state. The safety factor profile can be roughly estimated by tracing the magnetic field lines. The result is plotted in Fig. 13(c). It is worthy of notice that the central safety factor exceeds unity (up to 1.2), namely, the $q=1$ rational surface disappears. Therefore, it is quite reasonable that the system is stabilized with regard to the modes that are unstable at the initial condition, such as the $m/n=1/1$ and $2/2$ modes.
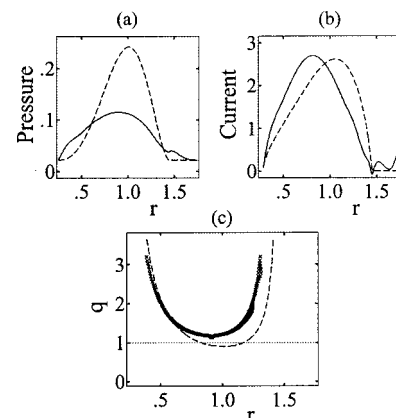

FIG. 13. Change in radial profiles of (a) pressure, (b) current, and (c) safety factor on the midplane. The broken line and the solid line [the cross markers in (c)] correspond to $t=0$ and $t=340\tau_A$, respectively.
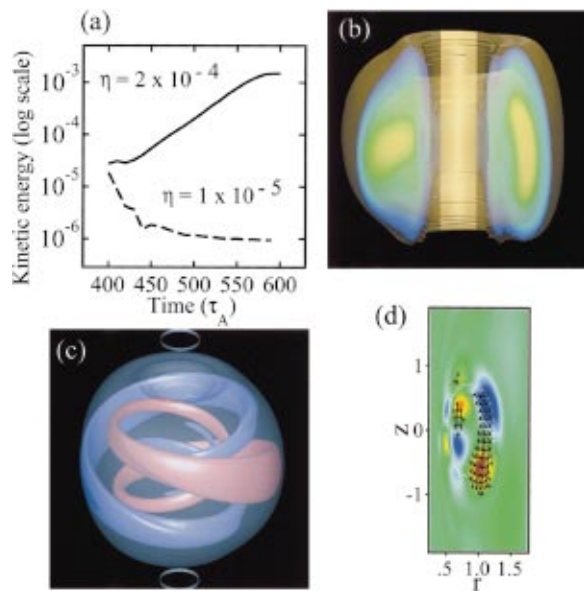
FIG. 14. (Color) (a) Dependence on the resistivity for the growth of the total kinetic energy in the latter stage of the simulation result. (b) Pressure profile at $t=500\tau_A$. (c) Three-dimensional mode structure in the second stage represented by iso-contour plots of the $n\neq0$ fluctuation in the pressure. Red and blue indicate the positive and the negative component, respectively. (d) Poloidal mode structure. The colored shade indicates the fluctuation in the pressure. The arrows denote the flow. The dotted line represents the location of the $q=2$ rational surface.

Though the system is ideally stable in this state for the modes which are linearly unstable in the initial equilibrium, the resistive modes become unstable due to the increase of the resistivity. The simulation is executed after $t=400\tau_A$ for two different resistivity terms, $\eta=1\times10^{-5}$ and 2×10^{-4}. The time development of the kinetic energy is plotted in Fig. 14(a). It shows that the perturbations actually grow for larger resistivity. The growth may be considered one which grows as the second step in the whole process. The configuration becomes a distorted one like Fig. 14(b). The mode structure for the second step is shown in Figs. 14(c) with a bird's-eye view of pressure fluctuations as well as poloidal mode patterns in the pressure. It can be seen that the $m=2/n=1$ mode is included as a dominant component for the second step. The location of the $q=2$ surface is also indicated in Fig. 14(d). The mode structure is mostly resonant to the $q=2$ surface, which shows the general nature of resistive modes.

IV. DISCUSSION

A. Comparison with experiments

In this section we compare the simulation results with the experimental observations of IREs. Figure 15 shows a temporal change in the radial pressure profile on the midplane in a fixed poloidal cross section, which can be compared with the experimental observations of the electron temperature or the density profiles reported in several papers.[2,12] The time scale of $1\,\tau_A$ for the simulation roughly corresponds to 0.5μsec for the experiments of START. It can be seen that the pressure profile suddenly collapses at around $t=200\tau_A$, while there is no visible change in the linear
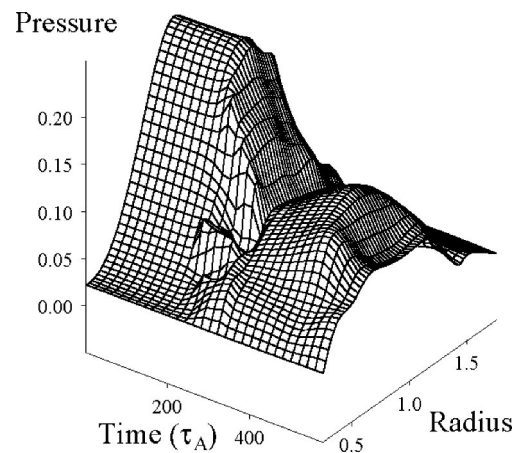

FIG. 15. Temporal change in radial pressure profile on the midplane in the simulation result.

stage. The time scale of the collapse is around $100\tau_A$. The pressure profiles are broadened to the edge during the collapse. These features are in good agreement with Fig. 10 of Ref. 12, which is the temporal variation in electron temperature and density profiles through an IRE measured using Thomson scattering.

The second step is also plotted in Fig. 15 for $\eta=2\times10^{-4}$. It can be seen that the excitation of the resistive mode leads to a two-step relaxation in the overall process, which agrees with the experimental observation as is denoted by IA and IB in Fig. 1.

The remarkable changes in the overall shape are compared with the CCD camera images introduced in Sec. I. The helical bright structure seen in Fig. 2(a) may be an instant phenomenon, since it is captured only when it is taken by a high time-resolution camera. The localized deformation described in Sec. III B corresponds to it with respect to the shape and the duration time scale. The conical layers appearing in Fig. 2(b) resemble the structure which appears right after the reconnection. To compare our simulation results with the CCD camera observations, in which the bright part mainly corresponds to the low temperature region, we reconstruct images using a volume rendering scheme to visualize the line-integrated intensity of plasma radiation. The radiation from the plasma is modeled in a simple way, in which the intensity of radiation per unit volume is assumed to be peaked when the local value of the pressure is around a certain low level. The images shown in Fig. 16 are thus created
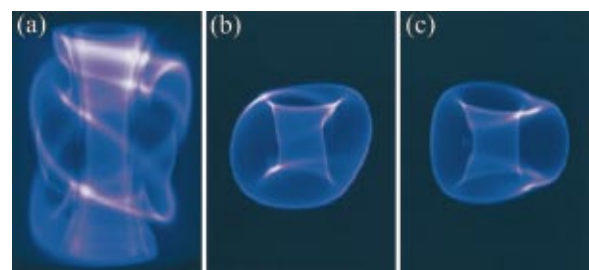

FIG. 16. (Color) Reconstructed image of the overall shape of the plasma from the simulation result.

by using the simulation results corresponding to Fig. 2. Figure 16(a) is drawn with the variables at $t=250\tau_A$. The conical structures are clearly recognized on the image as a bright part on the top and the bottom of the torus, and are in good agreement with Fig. 2(b). The bulk plasma, on the other hand, forms a spiral structure winding around the center rod as seen in Fig. 16. It also agrees with Fig. 2(b).

The $m=2/n=1$ distortion which grows in the second step is represented in Figs. 16(b) and 16(c). The only difference between them is the view angle, 90 deg. apart in toroidal angle. The tilt distortion and the fatness in only one side, which are seen in Figs. 2(c) and 2(d), are well reproduced in Figs. 16(b) and 16(c), respectively.

With regard to the toroidal current, there is no remarkable change in our simulation, although the system has experienced such a drastic change. This simulation is corresponding to the thermal quench phase, which is indicated with stage I in Fig. 1, and the toroidal current is not so increased in this stage in experiments, either.

Although the simulation cannot continue up to the current increase and the current quench phase, there is fairly good agreement between the simulation and the experiments. It supports the validity of our modeling.

B. Spontaneous phase alignment

The appearance of the localized bulge described in Sec. III B is a key point of this phenomenon in that it causes the collapse in pressure profile and the expulsion of the heat energy through the magnetic reconnection induced on it. Here we consider how the localized deformation is generated.

The most dominant mode in the linear stage is the $n=2$ mode; however, the deformation appears only in one side of the torus in the simulation result, as shown in Fig. 7. The reason why the number of the ridge of the deformation is reduced in the nonlinear stage is found to be the existence of the accompanying $m=1/n=1$ mode. We execute another simulation run to check the role of the $n=1$ mode in the nonlinear stage. This run is realized by artificially suppressing the growth of the $n=1$ mode. The result shows that two bulges originating from the $n=2$ mode are formed. It proves the necessity of the accompanying $n=1$ mode for the production of the single localized deformation.

The $n=1$ mode plays an additional role to the growth of the $n=2$ mode. Shown in Fig. 17 is the three-dimensional mode structure of the $n=1$ and the $n=2$ mode, respectively, where a pair of iso-surfaces for the negative (blue) and the positive (red) fluctuation components in the plasma pressure is plotted. It can be seen that the localized deformation observed in Fig. 7 is formed at the toroidal direction where the phases are aligned between the $n=2$ and the $n=1$ modes and the positive fluctuations are additional.

This phase-alignment mechanism among the excited modes, as is observed in Fig. 17, is a universal nature in the development of this phenomenon. Namely, the phases are spontaneously aligned to particular modes as a result of nonlinear interaction among them.[15] In order to confirm the nature of the spontaneous phase alignment, we execute a simu-
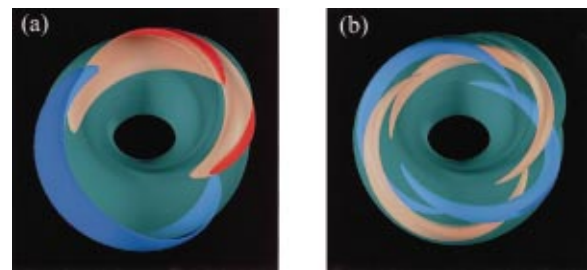

FIG. 17. (Color) The three-dimensional structure of the (a) $n=1$ and (b) $n=2$ component in the fluctuation in pressure at $t=195\tau_A$. The pictures are viewed from almost the top of the torus. The red and blue represent the iso-contour surfaces of fluctuation in pressure for a positive and a negative amplitude, respectively. The semitransparent surfaces denote an iso-contour of the net pressure. The localized deformation is lying on the right top of the pictures.

lation, in which the toroidal phase of the $n=1$ mode is initially shifted from that of $n=2$. In an axisymmetric system, the toroidal phase of each linear mode is determined by the perturbations given initially. Figure 18 is a top view of the torus and shows the time development of the fluctuations in the pressure on the midplane for $n=1$ and $n=2$. It is observed that the $n=2$ mode never changes the direction, while the $n=1$ mode is eventually split in two [Fig. 18(d)], and the outer one spontaneously rotates till it is aligned to the $n=2$ mode [Figs. 18(g) and 18(j)]. In this way, the localized deformation always appears in spite of the initial discrepancy among the phases.
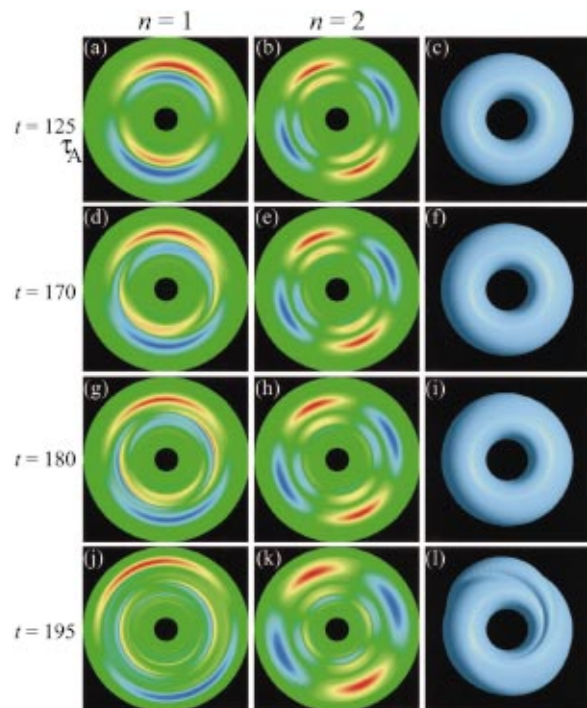

FIG. 18. (Color) Spontaneous phase alignment between $n=1$ and $n=2$ modes. The temporal change in the fluctuation in pressure on the midplane for the $n=1$ (left panels) and the $n=2$ (center panels) are drawn by colored shades. Corresponding change in overall shape is drawn in right panels by the top view of an iso-contour surface of the net pressure. The $n=1$ component gradually rotates until it is aligned with the $n=2$ mode. The localized deformation appears at the top in the panel.
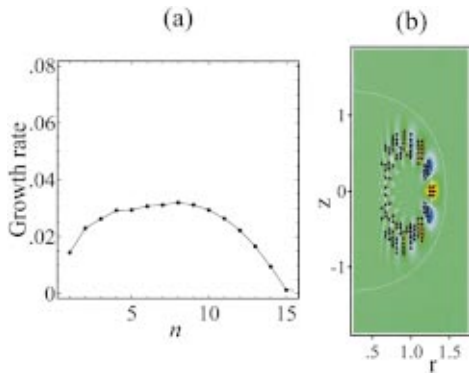
FIG. 19. (Color) (a) Same as Fig. 4(b) but for case B. (b) Same as Fig. 5 but for $n=8$ mode in case B. The dotted line indicates the location of $q=3/2$ surface.

C. Dependence on parameters

The linear instability described in Sec. III A is quite sensitive to the initial profiles. The existence of the $q=1$ surface especially causes the growth of the low n modes resonant to it such as $m=1/n=1$ and $m=2/n=2$. Here we investigate the nonlinear development when the $q=1$ surface does not exist. We have executed another simulation run, which we call hereafter case B, starting from an equilibrium where $q_0=1.06$, and other parameters are almost the same as those described in Sec. III, which is called case A.

The linear instability for case B is dominated by higher n modes than case A, such as $m=12/n=8$. These modes are identified as the ballooning modes by following the same procedure as described in Sec. III A. The figures corresponding to Fig. 4(b) and Fig. 5 for case B are shown in Fig. 19. As seen in Fig. 19(b), the poloidal mode structures are localized in the bad curvature region. The growth rate of those unstable modes for case B is much smaller than that of the dominant modes for case A.

It is worthy of notice that the nonlinear development for case B shows a quite similar behavior to that for case A. Namely, the localized deformation also appears in case B in the early nonlinear stage. In case B, however, the localized deformation consists of several small bulges, not a single one, as shown in Fig. 20. The occurrence of the spontaneous phase alignment described in Sec. IV B is difficult to recognize clearly in case B because of the small discrepancy in phases among the modes due to the high-n nature.

The development after that resembles case A. Namely, the magnetic reconnection between the internal and the ex-
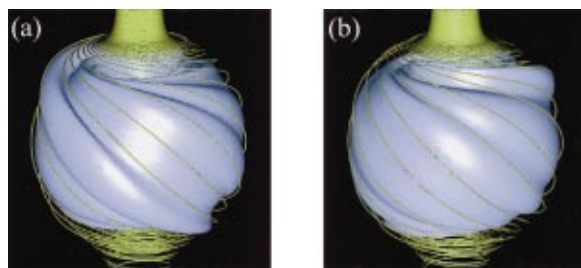

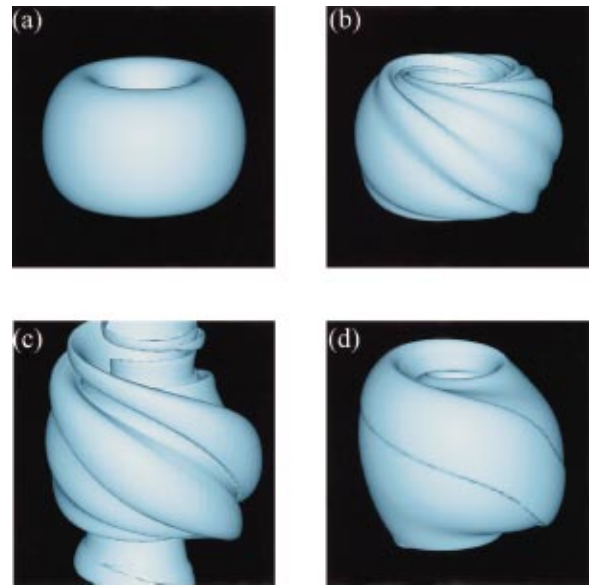FIG. 20. (Color) Same as Fig. 7 but for case B.

FIG. 21. (Color) Nonlinear time development of the three-dimensional structures of the plasma pressure for case B represented by iso-pressure surfaces. The time equals (a) 0, (b) 450, (c) 600, and (d) $825\tau_A$, respectively.

ternal field occurs at a couple of large bulges, and the characteristic conical shape appears at the top and the bottom of the torus. It should be noted that the magnetic reconnection occurs simultaneously at a couple of large bulges, as is seen in Fig. 21. After expelling part of plasma pressure out of the separatrix, the system becomes ideally stable. The stability for the resistive modes is similar to case A, that is, the $m=2/n=1$ distortion grows when we use a larger resistivity.

Hence, there is no significant difference in the nonlinear development between the cases A and B, except for the number of localized deformation. That is to say, an IRE can occur under such condition where q_0 is greater than unity.

V. CONCLUDING REMARKS

Nonlinear MHD simulations are performed to reveal the dynamical behavior of STs. It is found that multiple mode numbers of pressure-driven instabilities can be excited simultaneously in ST equilibria with the central safety factor close to unity. The nonlinear evolution of these instabilities shows the collapse of pressure profile in a short time scale by a convection motion. Localized deformation, which appears in the early nonlinear stage in consequence of couplings among the linear modes, leads the magnetic reconnection between the internal and the external magnetic field. The heat energy stored in the higher pressure region inside the separatrix is quickly ejected to the external region by strong plasma flow, which is induced along the reconnected field lines, much like a rubber ball which gets a hole on its surface. The torus is stabilized due to the change in the profiles, in particular, the safety factor profile and the decrease in plasma beta. However, a resistive $m=2/n=1$ mode still remains unstable.

The results are intensively compared with the experimental observations of START, and are in good agreement with them in several points as follows.

(1) The temporal and the spatial scales of the thermal quench.
(2) Large distortion of overall shape.
(3) Thermal quench proceeds in two steps, separated from increase in the current.

The second point is confirmed by experimental CCD images which show (1) appearance of a toroidally localized bulge, (2) formation of conical structures at the top and the bottom of the torus, and (3) growth of $m=2/n=1$ type helical distortion.

The results shown in this paper suggest the importance of the self-consistent dynamic analysis of the coupling between the internal and external region of a torus in understanding the mechanism of collapsing phenomena including the major disruptions for a conventional tokamak. Our conjecture is that when a torus has a mechanism to expel excessive heat energy quickly to the external region, the process can have a nature of resiliency like IRE, while the process becomes disruptive when the excessive heat energy remains inside long enough to destroy the configuration. Another topic that is raised by this simulation study is the necessity of a detailed analysis of the dynamics of the driven reconnection when there is a large pressure imbalance along reconnected field lines. In this simulation, the physics of heat conductivity along the magnetic field is not included. The parallel heat transport by electron conductivity is pretty large for high temperature plasma, while the perpendicular conductivity is negligible. The expulsion of stored energy to the external region would be enhanced if the conductivity were included in the model. The self-consistent treatment of such heat transport is a subject for future work.

ACKNOWLEDGMENTS

[1] A. Sykes, the START, NBI, MAST and Theory teams, Nucl. Fusion **39**, 1271 (1999)
[2] M. Ono, D. Stutman, Y. S. Hwang, W. Choe, J. Menard, T. Jones, E. Lo, R. Armstrong, M. Finkenthal, V. Gusev, S. Jardin, R. Kaita, J. Manickam, T. Munsat, R. Nazikan, and Y. Petrov, *Fusion Energy 1996* (International Atomic Energy Agency, Vienna, 1997), Vol. 2, p. 71.
[3] B. A. Nelson, T. R. Jarboe, D. J. Orvis, L. A. McCullough, J. Xie, C. Zhang, and L. Zhou, Phys. Rev. Lett. **72**, 3666 (1994).
[4] K. Hanada, T. Oikawa, K. Nozawa, H. Totsuka, K. Shimomura, E. Ishiyama, N. Shimoda, K. Yamagishi, and H. Toyama, in *Transactions of Fusion Technology* (American Nuclear Socity, 1995), Vol. 27, p. 440.
[5] R. Fonck, G. Garstka, T. Intrator, B. Lewicki, T. Thorson, R. Toonen, K. L. Tritz, B. White, and G. Winz, Bull. Am. Phys. Soc. **41**, 1400 (1996).
[6] A. Sykes, E. Del Bosco, R. J. Colchin, G. Cunningham, R. Duck, T. Edlington, D. H. J. Goodall, M. P. Gryaznevich, J. Holt, J. Hugill, J. Li, S. J. Manhood, B. J. Parham, D. C. Robinson, T. N. Todd, and M. F. Turner, Nucl. Fusion **32**, 694 (1992).
[7] M. Gryaznevich, R. Akers, P. G. Carolan, N. J. Conway, D. Gates, A. R. Field, T. C. Hender, I. Jenkins, R. Martin, M. P. S. Nightingale, C. Ribeiro, D. C. Robinson, A. Sykes, M. Tournianski, M. Valovic, and M. J. Walsh, Phys. Rev. Lett. **80**, 3972 (1998).
[8] T. C. Hender, S. J. Allfrey, R. Akers, L. C. Appel, M. K. Bevir, R. J. Buttery, M. Gryaznevich, I. Jemkins, O. J. Kwon, R. Martin, S. Medvedev, M. P. S. Nightingale, C. Ribeiro, C. M. Roach, D. C. Robinson, S. E. Sharapov, A. Sykes, L. Villard, and M. J. Walsh, Phys. Plasmas **6**, 1958 (1999).
[9] M. Ono and the NSTX Team, Nucl. Fusion (in press).
[10] M. Peng *et al.*, Nucl. Fusion (in press).
[11] R. Akers, T. C. Hender, P. J. Knight, O. J. Kwon, K. G. McClements, S. Medvedev, M. R. O'Brien, D. C. Robinson, S. E. Sharapov, G. Voss, and H. R. Wilson, Nucl. Fusion (in press).
[12] R. Akers, R. A. Bamford, M. K. Bevir, R. J. Buttery, A. Caloutsis, P. G. Carolan, N. J. Conway, M. Cox, G. F. Counsell, T. Edlington, C. G. Gimblett, M. Gryaznevich, T. C. Hender, I. Jenkins, O. J. Kwon, R. Martin, M. Mirinov, K. Morel, A. W. Morris, M. P. S. Nightingale, M. R. O'Brien, M. Peng, S. Petrov, P. D. Phillips, C. Ribeiro, D. C. Robinson, S. E. Sharapov, A. Sykes, C. C. Tsai, M. Tournianski, M. Valovic, and M. J. Walsh, *Fusion Energy 1996* (International Atomic Energy Agency, Vienna, 1997), Vol. 2, p. 57.
[13] M. Gryaznevich and A. Sykes, private communication, 1998–1999.
[14] R. J. Buttery, M. K. Bevir, A. Caloutsis, D. Gates, C. G. Gimblett, M. Gryaznevich, T. C. Hender, I. Jenkins, R. Martin, C. Ribeiro, D. C. Robinson, A. Sykes, M. Valovic, M. J. Walsh, and H. R. Wilson, in *Proceedings of the 23rd EPS Conference*, Kiev (European Physical Society, Petit-Lancy, 1996), Part I, p. 416.
[15] T. Hayashi, N. Mizuguchi, T. -H. Watanabe, Y. Todo, T. Sato, and the Complexity Simulation Group, Nucl. Fusion (in press).
[16] R. G. Kleva and J. F. Drake, Phys. Fluids B **3**, 372 (1991).
[17] W. Park, E. D. Fredrickson, A. Janos, J. Manickam, and W. M. Tang, Phys. Rev. Lett. **75**, 1763 (1995).
[18] R. G. Kleva and P. N. Guzdar, Phys. Rev. Lett. **80**, 3081 (1998).
[19] G. Bateman, *MHD Instabilities* (The MIT Press, Cambridge, MA, 1978).
[20] T. Sato and T. Hayashi, Phys. Fluids **22**, 1189 (1979).
[21] C. K. Birdsall and A. B. Langdon, *Plasma Physics via Computer Simulation* (McGraw-Hill, New York, 1985).